



**HAL**  
open science

## Monitoring of sow postural activity from 3D millimeter-wave radar imaging

Dominique Henry, Jean Bailly, Tiphaine Pasquereau, Jean-François Bompa, Hervé Aubert, Laurianne Canario

► **To cite this version:**

Dominique Henry, Jean Bailly, Tiphaine Pasquereau, Jean-François Bompa, Hervé Aubert, et al.. Monitoring of sow postural activity from 3D millimeter-wave radar imaging. *Computers and Electronics in Agriculture*, 2023, 213, pp.108214. 10.1016/j.compag.2023.108214 . hal-04219335

**HAL Id: hal-04219335**

**<https://laas.hal.science/hal-04219335>**

Submitted on 28 Sep 2023

**HAL** is a multi-disciplinary open access archive for the deposit and dissemination of scientific research documents, whether they are published or not. The documents may come from teaching and research institutions in France or abroad, or from public or private research centers.

L'archive ouverte pluridisciplinaire **HAL**, est destinée au dépôt et à la diffusion de documents scientifiques de niveau recherche, publiés ou non, émanant des établissements d'enseignement et de recherche français ou étrangers, des laboratoires publics ou privés.

## Highlights

### **Monitoring of Sow Postural Activity from 3D Millimeter-Wave Radar Imaging**

Dominique Henry, Jean Bailly, Tiphaine Pasquereau, Jean-François Bompa, Hervé Aubert, Laurianne Canario

- Postural activity of sows is monitored by using a millimeter-wave radar imaging system
- Sows are detected inside farrowing pens in presence of their piglets
- Millimeter-wave radar imaging system records heatmaps of the sow locomotor activity
- Millimeter-wave radar imaging system detects standing and lying postures

# Monitoring of Sow Postural Activity from 3D Millimeter-Wave Radar Imaging

Dominique Henry<sup>a,\*</sup>, Jean Bailly<sup>b</sup>, Tiphaine Pasquereau<sup>a</sup>, Jean-François Bompa<sup>a</sup>, Hervé Aubert<sup>c,d</sup>, Laurianne Canario<sup>b</sup>

<sup>a</sup>*INRAE GenPhySe, Castanet-Tolosan, 31326, France*

<sup>b</sup>*UE INRAE GenESI, Surgères, 17700, France*

<sup>c</sup>*LAAS-CNRS, Toulouse, 31400, France*

<sup>d</sup>*Toulouse University, Toulouse, 31000, France*

---

## Abstract

This paper presents a novel approach to monitor the postural activity of sows in farrowing pen using a millimeter-wave radar imaging system. Three-dimensional images of the scene are obtained from a 77GHz Multiple-Input Multiple Output radar and the mechanical scanning of the radar beam. We show that the processing of radar images based on the Cell-Averaging Constant False Alarm Rate allows detecting the standing and lying postures of sows despite the electromagnetic clutter. The experimental study reported here is performed from the monitoring of 16 sows from the Large White breed for a total of 46 hours. 3D positions of the sow are recorded and heatmaps of the sow locomotor activity are proposed. With few training radar data, we perform a classification of standing and laying postures with a mean balanced accuracy greater than 90%. The radar-based technique applied here in a cluttered environment inside farrowing pens may be extended to monitor pigs under other housing condition.

*Keywords:* animal behavior monitoring, millimeter-wave, precision livestock farming, sow activity, radar imaging, remote sensing.

---

## 1. Introduction

Animal behavior in livestock farming is a major concern for animal ethologists and biologists. This is particularly the case for pig farming in the

---

\*dhenry@laas.fr

European Community where new regulations for animal welfare are gradually being implemented. However, the well-being of pigs in livestock farming is difficult to define, but its measure requires usually the permanent monitoring and processing of behavioral data to correlate with physiological and environmental factors. In this context, the analysis of social interactions of sow with their piglets is particularly interesting. While most of them are very maternal with their piglets and move with caution and attention, some sows may crush piglets when they lie down, and the risk is higher in farrowing pens Edwards (2002). To limit the occurrence of these life-threatening events, a solution may consist of monitoring the behavior of many individual sows with their piglets inside the pens to detect the early warning signs of piglet crushing. The monitoring can be performed by recording data from various sensors. For example, accelerometers attached to the back of the sow were used to detect sitting, lying on the left or right side postures Canario et al. (2019); Ringgenberg et al. (2010). They can also be attached to neck collars to predict farrowing Pastell et al. (2016). However these sensors are embedded and may alter the behavior of the animals. Moreover, batteries of accelerometers need to be charged even if autonomy of such sensor can reach 5 days with a sampling rate of 10Hz Benaissa et al. (2019); Riaboff et al. (2022). Non-embedded remote monitoring of sow postural activities can be performed by using optical cameras. As an example, image processing techniques based on dynamic background extraction and optical flow was used to detect the activity changes in sows during final gestation Küster et al. (2020). Tracking of multiple pigs from two cameras with depth sensors were performed to detect behavioral changes Matthews et al. (2017). Different postures of sows were also detected from the processing of video recording based on deep learning approaches while kept in a farrowing crate Bonneau et al. (2021), or in a pen Zheng et al. (2018) in presence of piglets or in the days before farrowing Liu et al. (2022) and in correlation with nursing events Yang et al. (2018). These artificial intelligence algorithms were also applied to detect the posture of piglets Lu et al. (2022) and groups of pigs Xu et al. (2022). The posture budget and activity patterns predicted from convolutional neural network can then be correlated with, e.g., piglet survival and early growth, as shown in Girardie et al. (2023). These predictive methods provide accurate classifications, at the expense of a large number of annotated data in the training dataset. Moreover, the trained classifier must be as insensitive as possible to environmental changes, such as variations in brightness or observation angles.

On the other hand, remote monitoring sensors different than optical cameras exist and may offer other advantages. In particular, a promising

and very recent approach for livestock remote monitoring consists of using millimeter-wave radar. This technology is non-invasive (no installation on animals of wireless sensors or tags is needed). As it is the case in other radar applications, the echo detection relies on the electromagnetic field backscattered by the target. It may estimate the posture of animals directly from radar image processing and finally, allow detecting the position and the speed of animals (such as pigs or sheep) at tenth of meters from the radar. In the livestock welfare context (as described in, e.g., Ahmadi et al. (2011)) radar technology may be advantageously applied inside crates or pens or outside. As a proof of concept, a 24GHz Frequency-Modulated Continuous-Wave (FM-CW) radar was recently used for the first time by some of us to record the radar-to-sheep separation distance in a corridor Henry et al. (2018), while the displacement of sheep during behavioral tests were derived from the image processing obtained from a 77GHz Multiple-Input Multiple Output (MIMO) radar Dore et al. (2021). Doppler frequencies delivered by a 24GHz FM-CW radar were also measured to detect parturition of sows inside farrowing crates Manteuffel (2019) and a remote sensing solution using 122GHz FM-CW radars was investigated to detect the sow postural activity Dore et al. (2022).

In this paper we propose to extend the radar-based technique to the analysis of sow postural activity. Sows are with their piglets in farrowing pens in the so-called open configuration, in which they are not confined between metal fences but can freely move within an area of around 7-8m<sup>2</sup>. As the number of possible orientations of the sow's body is much higher in open configuration as compared to close configuration, the three-dimensional scanning of the radar beam in the farrowing pen is necessary to detect all possible postures and positions of sows. We use in this study a 77GHz FM-CW MIMO radar system that performs the 3D scanning of the radar beam. Electromagnetic waves in the millimeter-waves frequency band offer a larger modulation bandwidth than lower frequency bands, and a higher spatial resolution. The 3D beamsweeping is performed both mechanically and electronically in order to illuminate the entire farrowing pen. In order to identify the radar echoes associated with sows in the 3D images and mitigate the electromagnetic clutter, we propose a detection algorithm based on the Cell-Averaging Constant False Alarm Rate (CA-CFAR). CA-CFAR is a well-known radar detection algorithm that was applied recently to 3D radar images for the environment mapping Wang et al. (2022), drone detection Wang and Herschel (2022); Del-Rey-Maestre et al. (2021) and ship detection Kuang et al. (2020). We apply for the first time the algorithm to 3D radar images to detect the postures of a sow in a farrowing pen. Moreover, the

detections derived from the processing of 3D radar echoes are segmented by using a clustering algorithm. Clustering algorithms, such as DBSCAN which stands for Density-Based Spatial Clustering of Applications with Noise, are commonly applied in automotive industry Raj and Ghosh (2020) to detect various targets for example, in 77GHz radar images Wagner et al. (2016, 2017), or in 3D range/angle/Doppler images Palffy et al. (2020), Li et al. (2018). The novelty of the method we propose consists of applying the clustering on 3D elevation/azimuth/range radar images for livestock monitoring. Finally, the postures are classified using a conventional Quadratic Discriminant Analysis (QDA) Tharwat (2016) since only three features based on sow’s position are used to perform the classification.

The paper is organized as follows: Section II describes the experimental setup, the 3D radar imaging system and the measurement process. In Section III, the 3D scanning detection algorithm is detailed, including the description of the 3D CA-CFAR detection algorithm and the clustering technique for processing 3D radar images. Section IV analyses the results obtained from the monitoring of 16 sows for a total of 46 hours. The conclusion to this study is drawn in Section V, and some perspectives for future works are finally proposed.

## 2. Experimental Setup

### 2.1. 3D Radar Imaging System

The radar monitoring system is illustrated by the block diagram of Fig 1 (a). It includes the Frequency- Modulated Continuous-Wave (FM-CW) Multiple Inputs - Multiple Outputs (MIMO) radar commercialized by IN-RAS GmbH INRAS. This radar performs a 2D digital scanning of the radar beam, and delivers images where the coordinates of one pixel are given by the range of interrogation  $r$  and the azimuth angle  $\varphi$ . Another part of the system consists of an in-house mechanical platform attached to the radar. The platform performs the scanning in elevation of the radar beam. The elevation angle is denoted by  $\theta$ . Consequently, the monitoring system performs both a mechanical and digital scanning of the radar beam (see Fig 1 (b)).

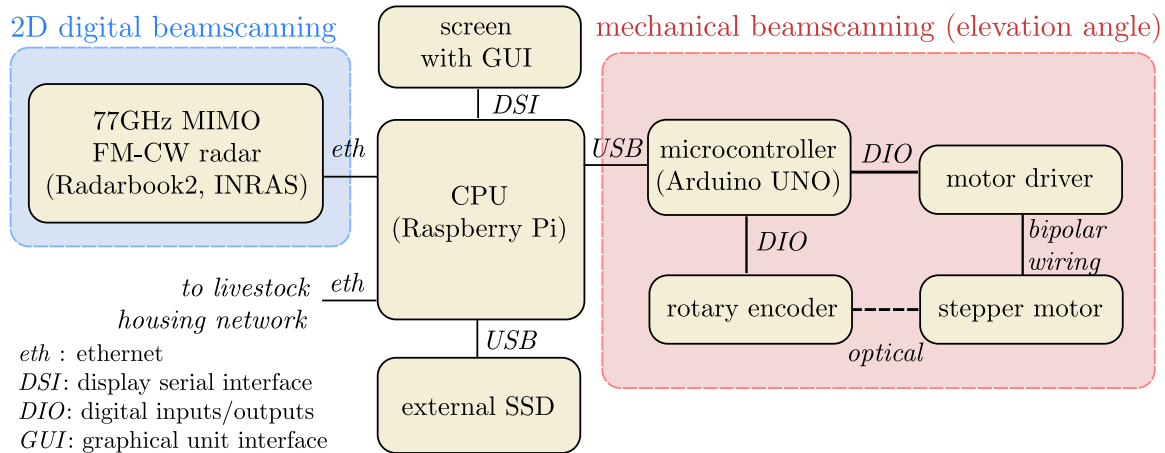
The main parameters of the radar system are listed in Table 1. The radar operates in the millimeter-waves frequency band at the carrier frequency of 77GHz. The so-called theoretical depth resolution  $d$  is defined by  $\frac{c}{2B}$ , where  $c$  is the speed of light in the vacuum and  $B(=2\text{GHz})$  denotes the modulation bandwidth of the chirp, that is, the bandwidth of the transmitted signal Piper (1993). Here  $d=7.5\text{cm}$ . The MIMO front-end of the radar is composed of 2 transmitting ( $T_X$ ) and 16 receiving ( $R_X$ ) channels, and also patch array

Table 1: Main Parameters of the proposed radar monitoring system

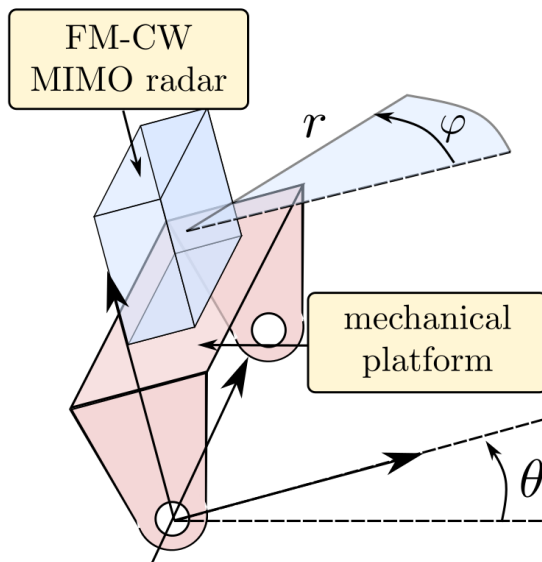
parameter	notation	value
carrier frequency	$f_c$	77GHz
modulation bandwidth	$B$	2GHz
depth resolution	$d$	7.5cm
up-ramp duration	$t_{up}$	256 $\mu$ s
down-ramp duration	$t_{do}$	64 $\mu$ s
gap duration between down and up ramps	$t_{gap}$	400 $\mu$ s
number of samples per up-ramp	$N_S$	512
repetition time	$t_{rep}$	50ms
output power	$P_{out}$	10dBm
number of $T_X$ channels	$N_T$	2
number of $R_X$ channels	$N_R$	16
$T_X$ antennas gain	$G_T$	17dBi
$T_X$ half-power elevation beamwidth	$\theta_{T,3dB}$	13.2°
$R_X$ antennas gain	$G_R$	15dBi
$R_X$ half-power elevation beamwidth	$\theta_{R,3dB}$	12.8°
radar x-position	$x_0$	-1.5m
radar y-position	$y_0$	$\pm 0.2$ m
radar z-position	$z_0$	1.8 $\pm 0.05$ m
maximal elevation	$\theta_{max}$	-20°
full-scale elevation range	$\Delta\theta$	60°
angular elevation speed	$v_\theta$	23.2°/s
ideal duration of one 3D scanning	$t_{scan,lin}$	2.5s
measured duration of one 3D scanning	$t_{scan}$	3.0s
angular elevation step	$\delta\theta$	1.2°
number of frames per 3D scanning	$N_{scan}$	1920

antennas are used as  $T_X$ - and  $R_X$ -antennas to estimate the directions of arrival of signals backscattered by the sow and piglets.

The radar system is placed in front of the farrowing pen at the position  $P$  ( $x_0, y_0, z_0$ ) defined in the Cartesian coordinates system ( $O, x, y, z$ ), where the origin  $O$  is placed at the center of the farrowing pen (ground level). We choose the radar position of coordinates  $x_0=-1.5$ m,  $y_0=\pm 0.2$ m and  $z_0=1.8\pm 0.05$ m in order to prevent damages of the radar setup from animals (sow and piglets) and the easy access to human operators. The schematic of the experimental setup with its open farrowing pen is shown in Fig 2. The pig is located at the point  $M$  of elevation/azimuth/range coordinates ( $\theta(t), \varphi(t), r(t)$ ) at time  $t$  in the coordinate system of origin  $P$ . The mechanical beamscanning in elevation is performed between minimal ( $\theta_{min}$ ) and maximal ( $\theta_{max}$ ) angles. Assuming a constant angular speed  $v_{\theta,min}$  between  $\theta_{min}$  and  $\theta_{max}$ , the duration  $t_{scan,lin}$  of one mechanical beamscanning (during one



(a)



(b)

Figure 1: (a) Block diagram of the 3D radar imaging system performing the digital beam-scanning of the scene in range and azimuth and (b) Schematic of the system performing the mechanical beamscanning in elevation

upward or downward scan of radar beam) is then given by  $\frac{\Delta\theta}{v_{\theta,lin}}$ . In our experiments, we select  $\theta_{min}=-80^\circ$  and  $\theta_{max}=-20^\circ$  to minimize the number of blind spots in the farrowing pen, and  $v_{\theta,lin}=24^\circ/s$ . Consequently, the duration  $t_{scan,lin}$  of the beam scanning is of 2.5s. However, the rotational speed is not constant in practice and consequently, as it can be observed in Fig 3, the measured elevation angle does not vary linearly over time. This non-linearity must be considered to accurately estimate the time  $t_{scan}$  required to scan the radar beam from  $\theta_{min}$  to  $\theta_{max}$  (or equivalently, from  $\theta_{min}$  to  $\theta_{max}$ ). This time (see Fig 2) is given by:

$$t_{scan} = \frac{\Delta\theta - 2\theta_e}{v_\theta} + 2t_e \quad (1)$$

where  $v_\theta$  denotes the measured angular speed,  $\theta_e$  is the measured angular interval in which the rotational speed is not constant during the time  $t_e$ . We measure  $v_\theta=23.2^\circ/s$ ,  $\theta_e=1^\circ$  and  $t_e=250ms$ . Therefore, the time  $t_{scan}$  required to scan the radar beam from  $\theta_{min}$  to  $\theta_{max}$  is then of 3.0s.

Moreover, the radar delivers  $N_T \times N_R$  signals with a full repetition time  $t_{rep}=50ms \geq N_T \times (t_{up} + t_{do} + t_{gap})=1.4ms$ . The angular elevation step  $\delta_\theta=1.2^\circ$  of a 3D radar image generated during the radar beam at the constant rotational speed  $v_\theta$  from  $\theta_{min}$  to  $\theta_{max}$  (or from  $\theta_{max}$  to  $\theta_{min}$ ) is then:

$$\delta_\theta = v_\theta \times t_{rep} = \frac{\Delta\theta - 2\theta_e}{t_{scan,lin}} \times t_{rep} \quad (2)$$

with  $t_{rep}=50ms$ . With such value, blind spots in elevation are prevented by choosing a value for  $\delta_\theta$  lower than the half-power beamwidth of the  $T_X$  radar antennas  $\theta_{T,3dB}$ . Moreover, the number of registered frames per scan is defined by:

$$N_{scan} = \lceil N_T \times N_R \times \frac{t_{scan}}{t_{rep}} \rceil \quad (3)$$

where  $\lceil . \rceil$  denotes the ceil function. The number of frames per 3D scanning  $N_{scan}$  is 1920. Values and descriptions of the scanning parameters are summarized in Table 1.

## 2.2. Measurement Protocol

The measurements are performed at the experimental breeding unit of INRAE GenESI, France. The experiment authorization number of the experimental farm GenESI (Pig phenotyping and Innovative breeding facility, <https://doi.org/10.15454/1.5572415481185847E12>) is A-17-661. The experiment was designed in compliance with Legislations of the European Union

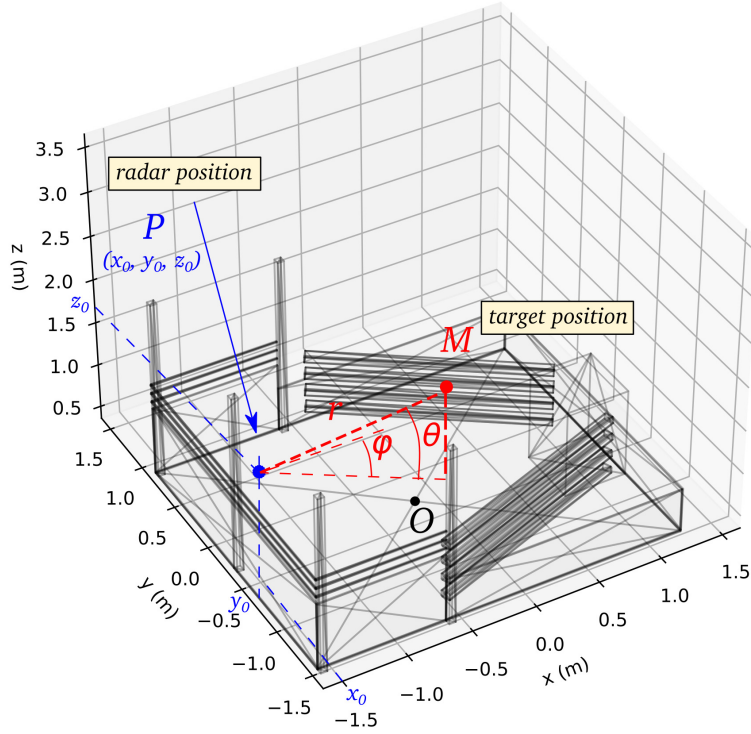


Figure 2: Schematic of the farrowing pen in open configuration with both Cartesian  $(O, x, y, z)$  and radar  $(P, \theta, \varphi, r)$  elevation / azimuth / range coordinates systems.

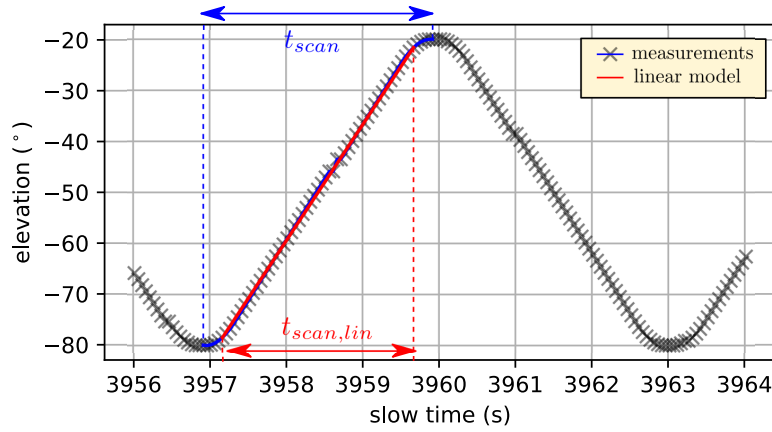


Figure 3: Variation of the measured elevation angle of the radar beam as a function of slow time.

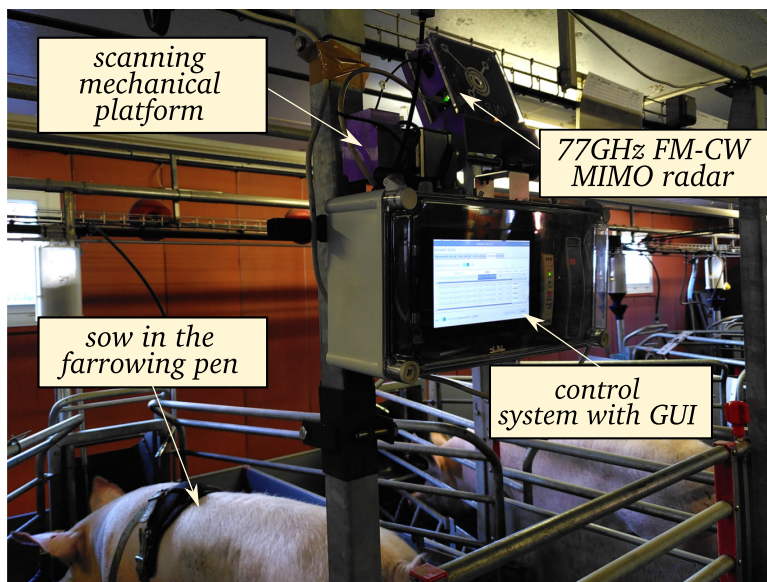


Figure 4: Photograph of the experimental setup. The 3D beamscanning system is located above the farrowing pen.

(Directive 86/609/EEC) and France (Decree 2001-464 29/05/01) for the care and use of animals (Agreement For Animal Housing Number C-35-275-32). It was approved by the ethical committee of the Nouvelle Aquitaine Regional Council (authorization #15563-2018060113088001). A picture of the experimental setup is shown in Fig 4. The 3D scanning of the radar beam is launched during 2-3 hours for different sows of the Large White breed with piglets aging from 7 to 15 days. All farrowing pens are quasi-identical, but some pens are symmetrically reversed along the x-axis. In the photograph, the device attached to the sow is an accelerometer used in another study. It is not involved in the reported work. The setup calibration is achieved from scanning the farrowing pen in absence of sow and piglets. The resulting 3D reference images are used in post-processing to remove undesirable radar echoes called the *clutter* which are generated by the electromagnetic backscattering of motionless objects placed in the sow environment, such as the metallic fences, the ground, the sow trough and piglets' feeding trough. For this development, 16 different sows are monitored for a total of 46 hours. For comparison purpose, videos of the farrowing pens are recorded during the radar scanning of the scene. Sow postures are annotated manually for all video records and considered here as the ground-truth of sow postures.

Table 2: Monitored Sows

sow id	date	duration	x-axis	cal. <sup>a</sup>	use <sup>b</sup>
015203	08-17-2022	120 min	rev.	no	training
015236	08-18-2022	120 min	rev.	no	training
113911	08-18-2022	120 min	rev.	yes	training
014648	08-19-2022	120 min	-	no	training
011656	11-08-2022	120 min	-	yes	test
011696	11-08-2022	180 min	rev.	yes	test
011831	11-09-2022	180 min	-	yes	test
011863	11-09-2022	180 min	rev.	yes	test
012423	11-09-2022	180 min	-	yes	test
012962	11-10-2022	180 min	rev.	yes	test
011689	11-21-2022	180 min	-	yes	test
011762	11-21-2022	180 min	rev.	yes	test
011786 <sup>c</sup>	11-22-2022	180 min	-	yes	test
014794	11-22-2022	180 min	rev.	yes	test
011796	11-23-2022	180 min	-	yes	test
014867	11-23-2022	180 min	-	yes	test
011786 <sup>c</sup>	11-24-2022	180 min	-	yes	test

*a* : calibration performed without sow and piglets.

*b* : use for the QDA classification (see Section 4.2)

*c* : sow 011786 has been monitored twice.

rev. : the farrowing crate is symmetrically reversed along the x-axis.

### 3. 3D Scanning Detection Algorithm

#### 3.1. Generation of the 3D radar images

Prior to the application of the detection algorithm, 3D images are generated from the recorded radar raw data. Raw data are 3D matrices of size  $N_S \times N_C \times N_L$ . As referred in Section 2.1,  $N_S$  is the number of samples of the fast time axis.  $N_C = N_T \times N_R$  is the number of signals per combined  $T_X$  and  $R_X$  channels of the channel axis.  $N_L$  is the number of samples of the slow time axis. Raw data are then converted into consecutive 3D radar images in the coordinate system  $(P, \theta, \varphi, r)$  as a function of the slow time. Here are the following steps of the processing:

- Step 1 in Fig 5: we apply a Hanning window to reduce side lobes of echo level, and a FFT (Fast Fourier Transform) along the fast time axis on raw data. We keep only the first half of the resulting (symmetric) spectrum. We obtain beat frequency spectra of  $\frac{N_S}{2}$  samples of echo level as a function of the distance  $r$ . We can choose a maximum distance value  $r_{lim}$  to reduce the number of samples. This number is then  $N_{S,lim} = \lfloor \frac{r_{lim}}{d} \rfloor$ , where  $\lfloor \cdot \rfloor$  denotes the floor function. We choose  $r_{lim} = 5.0\text{m}$  and  $N_{S,lim} = 66$ . The 3D matrix is now of size  $N_{S,lim} \times N_C \times N_L$ ;
- Step 2 in Fig 5: we multiply each row of the 3D matrix channel axis by the corresponding calibration complex value provided by the radar manufacturer. Next, we apply a second Hanning window and FFT along the channel axis to perform a digital beamscanning. Zero-padding of factor  $n_p = 8$  is applied and the number of samples of the resulting azimuth axis is then  $N_\varphi = n_p \times N_C = 256$ . Consequently, we obtain a complex-values  $N_{S,lim} \times N_\varphi \times N_L$  matrix. Moreover, the azimuth angle computed from the FFT beamforming is defined by  $\varphi(k) = \arcsin(-1 + \frac{k}{N_\varphi})$ , with  $k = 0..N_\varphi - 1$ ;
- Step 3 in Fig 5: indexes ranging from 0 to  $N_L - 1$  are associated with the timestamp of the local network recorded for each radar data acquisition, as well as the elevation angle. We then split on the slow time axis the 3D matrix into sub-matrices at indexes that correspond to elevation angles  $\theta_{min} = -80^\circ$  and  $\theta_{max} = -20^\circ$ . Values of sub-matrices that are split from  $\theta_{max}$  and  $\theta_{min}$  are reversed along the slow time axis. In order to have sub-matrices of same dimensions, we perform a spline interpolation along the slow time axis by using the elevation vector ranging from  $\theta_{min}$  and  $\theta_{max}$  with the angular step  $s_\theta = 2.4^\circ$ . Note that

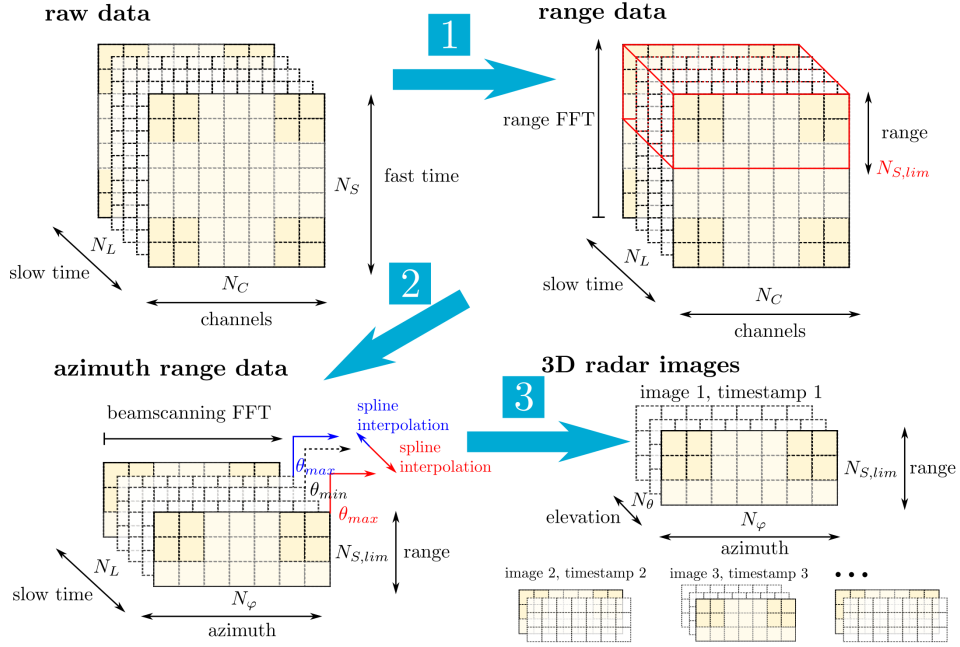


Figure 5: Schematic of the algorithm that generate 3D radar images from raw data.

$s_\theta$  must be greater than  $\delta_\theta$ . We finally obtain the elevation axis with a number of samples given by  $N_\theta = \lfloor \frac{\Delta_\theta}{s_\theta} \rfloor = 25$ .

From the above-described steps, we obtain 3D radar images of dimensions  $N_\theta \times N_\varphi \times N_{S,lim}$  with their associated timestamps.

### 3.2. Radar Detection Algorithm

Once the 3D radar images are generated, we apply an algorithm to detect the sow position  $(x, y, z)$  inside the farrowing pen. The detection algorithm is based on the Constant False Alarm Rate (CFAR) algorithm applied to 3D radar images. The algorithm is composed of several steps (see also the schematic displayed on Fig. 6), as well as the video in supplementary data in Appendix A:

- We compute the detection threshold of the CA-CFAR algorithm for each voxel of a single 3D calibration image (that is, in absence of sow and piglets in the farrowing pen). We choose here a CA-CFAR (Cell Averaging CFAR) algorithm Richards (2014) where the detection

threshold is given by:

$$\hat{T} = \frac{\alpha}{N_w} \sum_{i=1}^{N_w} v_i \quad (4)$$

where  $N_w$  designates the number of reference cells for which the averaging is performed,  $v_i$  denotes the echo level value of the reference cell, and  $\alpha$  is the threshold multiplier defined by:

$$\alpha = N_w(\text{pfa}^{-\frac{1}{N_w}} - 1) \quad (5)$$

pfa is the probability of false alarm. Dimensions  $(n_\theta, n_\varphi, n_r)$  of the 3D averaging window around one voxel is (5,5,5) without guarding cells. The number of reference cells is then  $N_w = n_\theta \times n_\varphi \times n_r - 1 = 124$ . As the optimal PFA leading to a maximum of true detections is unknown, the set of 3D detection thresholds with PFA ranging from  $10^{-7}$  to  $10^{-2}$  is generated;

- We define here *detections* as voxels with echo level greater than the detection threshold  $\hat{T}$ . We compute detections in the 3D radar images while increasing PFA until the minimal number of detections  $n_{min}$  is reached. We choose here  $n_{min}=100$  (we may also choose higher values of  $n_{min}$  for display purposes, as illustrated in Fig 7 for  $n_{min}=400$ );
- We check the detections in order to know if they correspond to the same pig. For this purpose, we compute the separation distances between detections and create groups of close detections from the mean-shift *clustering* algorithm Comaniciu and Meer (2002) developed in Pedregosa et al. (2011). Within a single 3D radar image, we obtain one (or more) cluster(s) composed of voxels. Clusters for which the number of voxels is lower than  $n_{lim}=10$  are discarded;
- We convert the elevation/azimuth/range coordinates of the selected voxels into Cartesian coordinates in the  $(O, x, y, z)$  system. In this transformation, the radar coordinates  $(x_0, y_0, z_0)$  are involved;
- We compute the coordinates  $(x_G, y_G, z_G)$  of the barycenter of each cluster. The clusters for which the barycenter is outside the farrowing pen boundaries are discarded. We also remove clusters for which  $z_G$  is greater than the maximal height of the studied sows  $z_{lim}=1.1\text{m}$ ;
- We compute the coordinates of the barycenter of remaining clusters. We assume that a set of clusters corresponds to the same target if the distances between constitutive clusters are smaller than  $d_{lim}=1.0\text{m}$ ;

- If several sets of clusters remain after the above-described steps, we consider that the set composed of the highest number of voxels corresponds to the radar echoes of the sow.

For illustration purposes, two examples of cluster set with  $n_{min}=400$  are displayed in Fig 7 for sow 011863 in the farrowing pen. In the first case (a - b), the sow is in the standing posture and the set of clusters is composed of two clusters (blue squares). The red cross designates the coordinates of the barycenter. In the second example, the sow is lying on the side with udder exposed and nursing the piglets, and the set of clusters is then composed of one cluster close to the ground level and one on the pen door. In such posture, the value of  $\theta$  must be very close to  $\theta_{min}=-80^\circ$  to detect the sow.

### 3.3. Features of 3D Clusters

Features of 3D clusters computed in Section 3.2 are used to detect the postural activity and trajectories of the sow. Features of the set of 3D clusters, such as the barycenter coordinates  $(x_G, y_G, z_G)$ , the number of voxels, and the level of radar echo, are computed as a function of the slow time. As an example, features  $x_G, y_G$  and  $z_G$  of sow 011863 are displayed in Fig 8 (black crosses). We observe two time slots: between 500s and 5000s the sow does not move, is lying and nursing, and after 5000s, an active period of standing in motion is observed. In order to remove false detections, and to increase the signal-to-noise ratio, we apply a mean filter to features  $x_G, y_G$  and  $z_G$  with a sliding window of size 10 (which corresponds to a duration of around 30s). We obtain trajectories (blue lines) with filtered false detections (easily visible for example for feature  $x_G$ ). If there is no detection at a given time bin, we compute the position as the average between the previous and next estimations of the position.

## 4. Results and Discussion

### 4.1. Moving and Stationary States

We apply the filtered feature  $z_G$  detailed in Section 3.3 to detect moving or motionless sow from the computation of the time derivative of  $z_G$  (that is, the speed  $\dot{z}_G$ ). By defining a threshold  $\dot{z}_0$ , the condition  $|\dot{z}_G| > \dot{z}_0$  corresponds to a motion of the sow while the condition  $|\dot{z}_G| \leq \dot{z}_0$  corresponds to a motionless state. This result is illustrated in Fig 9 with the filtered  $z_G$  that was previously computed from the threshold  $\dot{z}_0=2.5 \times 10^{-3} \text{m.s}^{-1}$ . Motion and motionless states are enlightened respectively in blue and orange colors in the Figure, and we can easily observe the sow motion after 5000s.

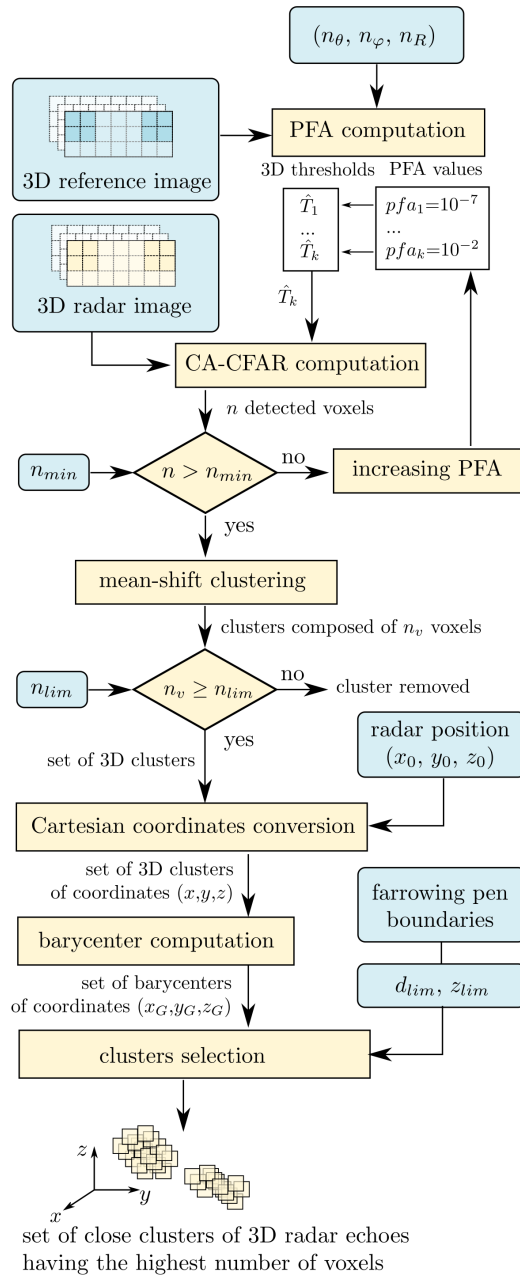
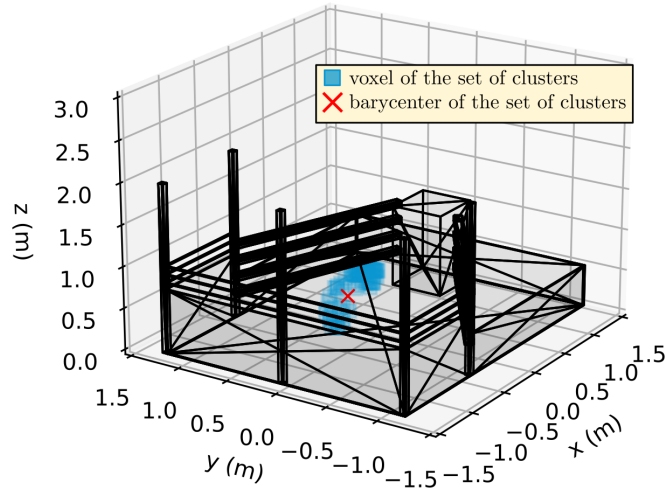


Figure 6: Schematic of the radar detection algorithm

Wed Nov 9 12:00:32 2022

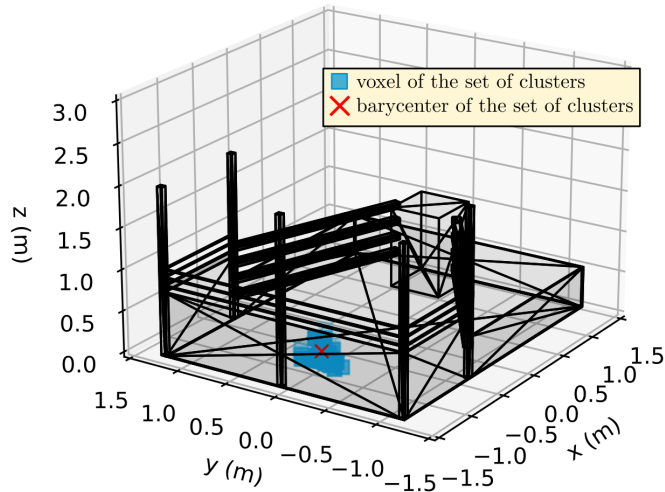


(a)



(b)

Wed Nov 9 12:33:49 2022



(c)



(d)

Figure 7: Set of 3D clusters ( $n_{min}=400$  voxels) and corresponding video frames of sow 011863 in the farrowing pen for (a - b) a "standing" posture and (c - d) a "lying on the side with udder exposed" posture.

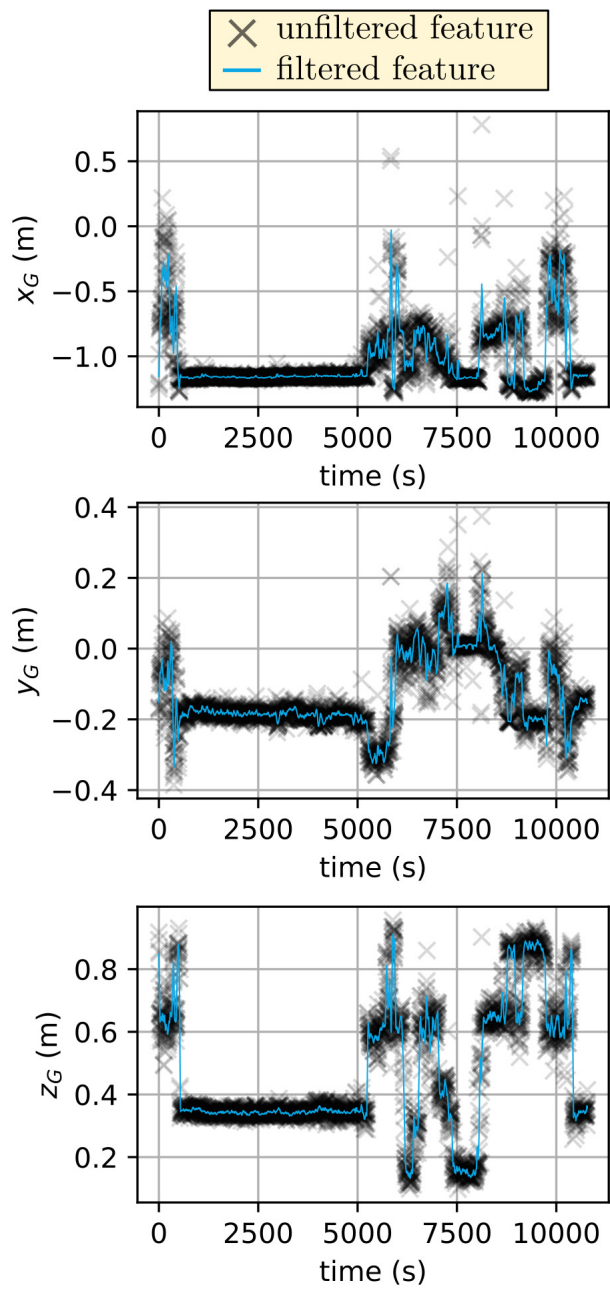


Figure 8: Unfiltered (black crosses) and filtered (blue lines) features  $x_G$ ,  $y_G$  and  $z_G$  as a function of the time (sow 011863).

Therefore, we can define a criterion of motion along the spatial axis  $z$  as follows:

$$\gamma_z(\dot{z}_0) = \frac{T(|\dot{z}_G| > \dot{z}_0)}{T} \quad (6)$$

where  $T$  denotes the total measurement duration, and  $T(|\dot{z}_G| > \dot{z}_0)$  designates the measurement duration when  $|\dot{z}_G| > \dot{z}_0$ . If the sow is continuously motionless, we obtain  $\gamma_z(\dot{z}_0)=0$ . Inversely, if the sow moves continuously, then  $\gamma_z(\dot{z}_0)=1$ . The same definition may be applied for axes  $x$  and  $y$ .  $\gamma_x$ ,  $\gamma_y$  and  $\gamma_z$  are plotted respectively in green, orange and blue colors in Fig 10 for all monitored sows (see Table 2) with the threshold of  $2.5 \times 10^{-3} \text{m.s}^{-1}$ . We observe high variability in moving activity between sows. For instance, sow 113911 is moving frequently, whereas sow 011762 is motionless during the experiment. Moreover,  $\gamma_x$  has mostly greater values than  $\gamma_y$  and  $\gamma_z$ , because the sow can move more along the x-axis in the farrowing pen.

2D heatmaps of  $x_G$  and  $y_G$  may also be useful to detect recurrent positions of the sow inside the farrowing pen. These heatmaps are 2D histograms representing  $(x,y)$  regions where sows are detected during the scanning of the radar beam. In Fig 11 are displayed heatmaps of  $x_G$  and  $y_G$  of (a) sow 113911 and (b) sow 011762. Heatmaps are computed over cells of size  $30\text{cm} \times 30\text{cm}$  and blue to yellow colors represent the normalized values of the  $(x, y)$  histogram ranging from 0 to 1. Even if the estimation of the position is coarse (we do not actually know which part of the sow is detected), we observe heatmap differences between animals. As observed previously with the computation of  $\gamma_x$  and  $\gamma_y$ , sow 011762 remains in a more constrained space than sow 113911, with a heatmap on the specific spot  $(x=-1.2\text{m}, y=-0.2\text{m})$  close to the door of the farrowing pen. Inversely, the heatmap associated with sow 113911 indicates more spreading motion.

#### 4.2. Postural Activity

In this section, we study the postural activity of the sows by using the filtered features  $x_G$ ,  $y_G$ ,  $z_G$  defined in Section 3.3. We consider three classes of postures. The first class is called "*standing*" and includes the "*standing*" posture (as depicted in Fig 7.b). The second class is called "*transitions*" and it groups "*kneeling*" and "*sitting*" postures. The last group is called "*lying*", and it includes postures for which the sow is lying : "*lying sternally*", "*lying on left side*", "*lying on right side*", and "*lying with udder exposed*" or not. Postures are annotated manually from the video recording by a single observer and the corresponding ethogram is reported in Girardie et al. (2023). Feature  $z_G$  is plotted as a function of  $x_G$  in Fig 12 for "*standing*" (green), "*transitions*" (orange) and "*lying*" (blue) postures for all sows (see

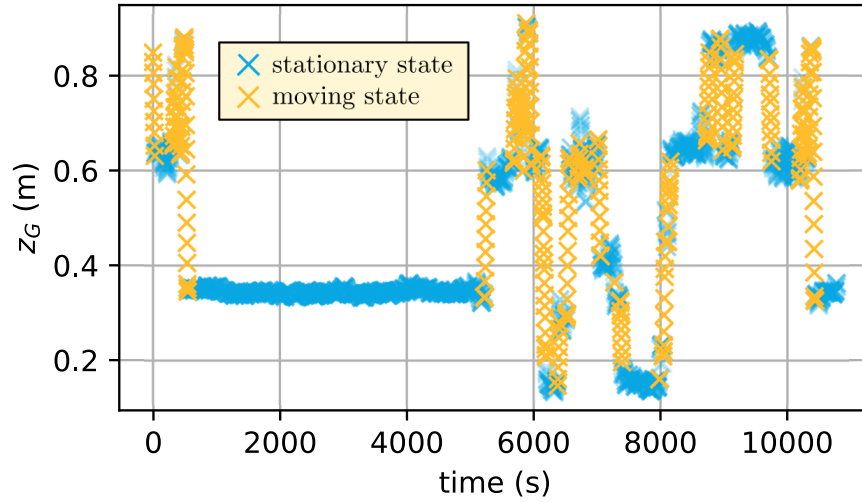


Figure 9: Stationary (blue) and mobile (orange) states of feature  $z_G$  for threshold  $\dot{z}_0=2.5 \times 10^{-3} \text{m.s}^{-1}$  (sow 011863)

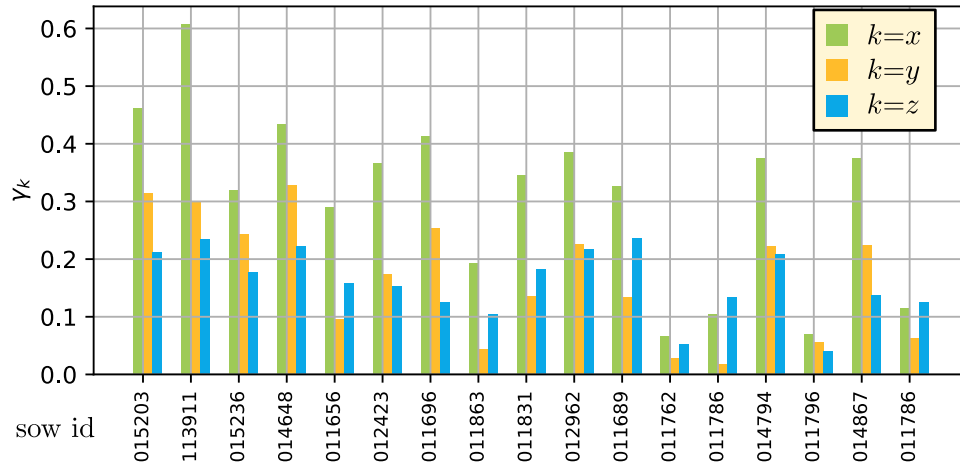


Figure 10: Criteria of motion  $\gamma_k$  for  $k=x$  (green),  $y$  (orange) and  $z$  (blue) for a threshold  $\dot{k}_0=2.5 \times 10^{-3} \text{m.s}^{-1}$

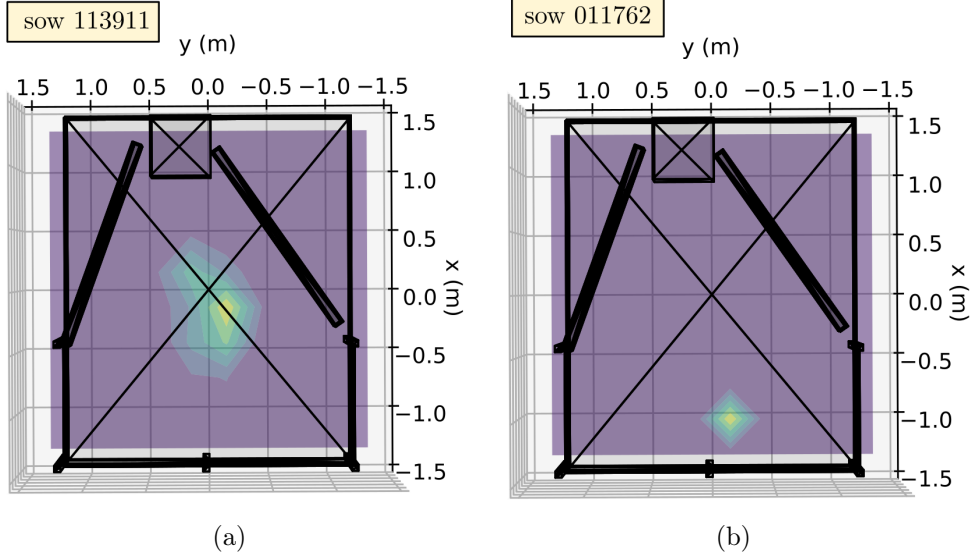


Figure 11: 2D Heatmaps of  $x_G$  and  $y_G$  for (a) sow 113911 and (b) sow 011762. Blue to yellow colors are normalized  $(x,y)$  histogram values ranging from 0 to 1.

Table 2). We observe that postures depend on  $z_G$ . Lying postures correspond to small values of  $z_G$  (i.e., lower than 0.4m) while "*transition*" and "*standing*" postures are given for  $z_G$  higher than 0.4m. However, the "*transition*" and "*standing*" postures are difficult to distinguish, because the head or back of the animal can be at the same height when the sow is "*standing*", "*kneeling*" or "*sitting*". Moreover, we note some isolated sets of data that correspond to false detections, which might be due to the rare detection of human operator in the scene during the experiment. If they entered the pen, it was for a few seconds only. Finally, we observe that  $x_G$  and  $z_G$  are slightly correlated (Pearson correlation coefficient of -0.40) for "*standing*" and "*transition*" postures. This correlation is due to a bias of the elevation angle before the conversion into Cartesian coordinates (see Section 3.2).

Next, we monitor the postural activity of the sow from the classification based on a standard QDA classification using two classes: "*standing and transition*" (class 0) and "*lying*" (class 1). Data used for the classification are time filtered features  $x_G$ ,  $y_G$  and  $z_G$  at motionless state (see Section 4.1). For training data, we use the measurement results obtained in August 2022 from the monitoring of 4 sows for a total of 8 hours. According to range values of features  $x_G$ ,  $y_G$  and  $z_G$ , a QDA should be sufficient for the proposed classification to distinguish between "*lying*" and "*standing and transition*"

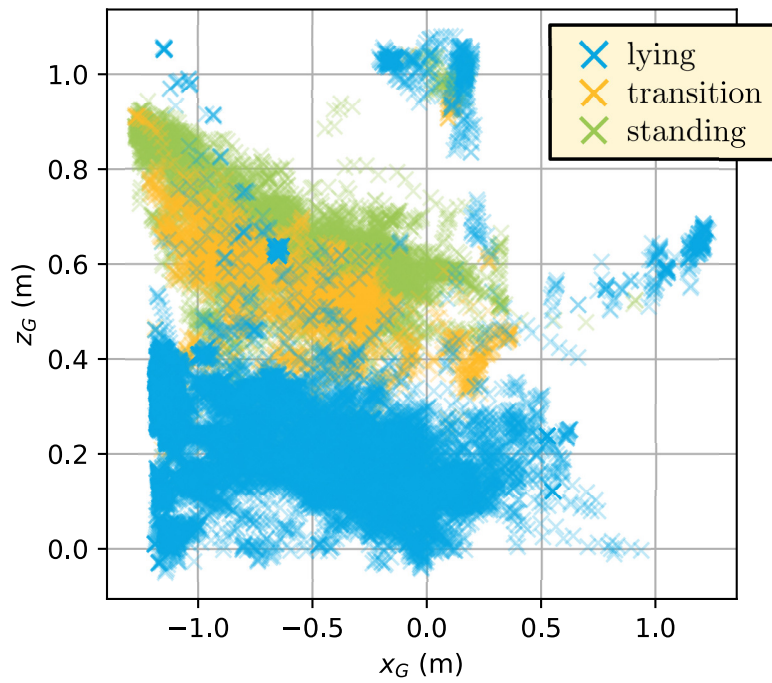


Figure 12: Feature  $z_G$  as a function of  $x_G$  for all monitored sows (46 hours of recording for 16 animals) for "standing" (orange), "transition" (green) and "lying" (blue) postures.

Table 3: Confusion Matrices of Sows Postural Activity

		predicted			
		<b>0</b>	<b>1</b>	<b>0</b>	<b>1</b>
observed	<b>0</b>	1679 (84.3%)	312 (15.7%)	6286 (88.3%)	828 (11.7%)
	<b>1</b>	183 (3.6%)	4923 (96.4%)	556 (2.1%)	26686 (97.9%)
		<i>training data</i>		<i>tested data</i>	

class 0 : "*standing and transition*"; class 1 : "*lying*"

postures. With such classification and considering the amount of data, the risk of overfitting is low (in comparison with other classifications such as RandomForest or AdaBoost). Moreover, if the radar position is correctly estimated and the height of the sows does not vary too much, the number of training data for the classification should be sufficiently high. Data for the test are the remaining measurement results of Table 2 obtained from the monitoring of 12 sows for a total of 38 hours. Results of the classification are reported in Table 3 for training and tested data. We obtained encouraging results for different sows and dates of experiment, with precision and sensitivity (recall) of respectively 88.3% and 90% for the "*standing and transition*" class, and 97.9% and 98% for the "*lying*" class. Note that precision is defined by  $\frac{TP}{TP+FP}$  and sensitivity by  $\frac{TP}{TP+FN}$ , with  $TP$ ,  $FP$  and  $TN$  the number of True Positives, False Positives and True Negatives. The balanced accuracy of the tested data, defined by  $\frac{1}{2}(\frac{TP}{TP+FN} + \frac{TN}{TN+FP})$  is equal to 95%. Confusion matrices of postures for each sow are also displayed in Fig 13 and variation in the precision is observed between animals. As an example, the precision obtained for the "*standing and transition*" class for sow 113911 is 74%, whereas it reaches 100% for sow 011689. Such difference is explained by the difficulty to class a number of transition postures (that is, "*sitting*" and "*kneeling*") in the "*standing and transition*" class instead of the "*lying*" class. For this proof of concept, there is sufficient data to show that two postures can be detected (standing and lying) with the proposed classification method. However, more data may be required if other learning methods are employed (such as convolutional neural networks), or if the measurements are performed in more complex environments.

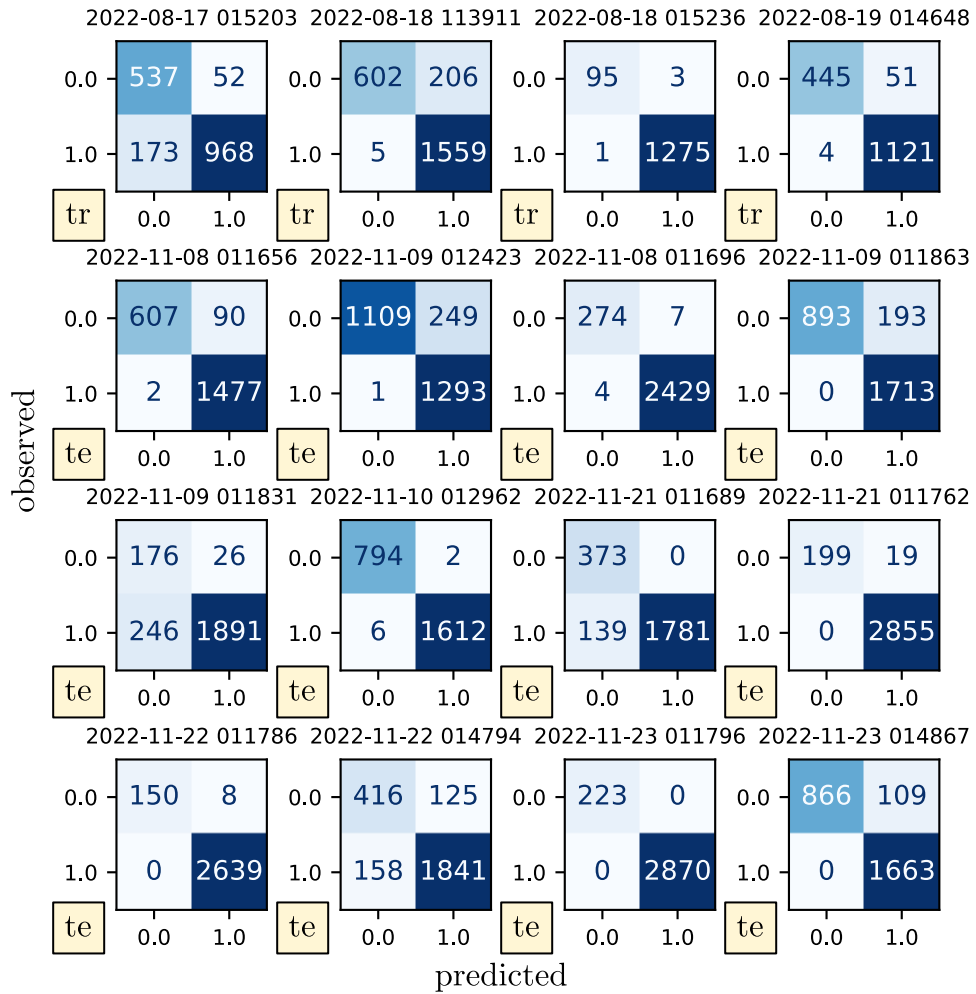


Figure 13: Confusion matrices of postural activity for each sow; class 0 : standing and transition; class 1 : lying; *tr* : training data; *te* : tested data.

### 4.3. Discussion

#### 4.3.1. Postural activity monitoring and potential improvements

The proposed monitoring of sow postural activity by using 3D millimeter-wave radar images presents very encouraging results. We obtain good classification results with few training data to distinguish between "lying" postures and "standing and transitions" postures for different sows and dates during this radar experiment. And we proceed to the accurate estimation of the averaged height  $z_G$  of the sow. Moreover, the radar system also predicts the position of the sow, and other coordinates  $x_G$  and  $y_G$  may offer useful information. As an example, motionless and moving states can be extracted and (x,y) heatmaps of the sow inside the farrowing pen can be plotted to enlighten different behaviours. Nevertheless, "transition" postures (i.e., "kneeling" and "sitting") are difficult to detect, because the head and back of sow are not distinguishable by the radar, and because the height  $z_G$  presents high variability for these postures. Moreover, "transition" postures are far less used than other postures, which limited our capacity to train the algorithm on these behavioral items. In addition, technical solutions can be proposed to improve the radar monitoring of the postural activity, such as increasing the bandwidth  $B$  of the radar to enhance the depth resolution and improve the 3D grid resolution (mainly, the  $x$  and  $z$  coordinates), or else finding the optimal radar position  $(x_0, y_0, z_0)$  to minimize the ambiguities of postural detection, increasing the number of radars to remove eventual blind spots, improving the slow time resolution from higher angular speed  $v_\theta$  and decreasing the repetition time  $t_{rep}$ , and/or, replacing the mechanical scanning of the radar beam with a full 3D digital beamscanning system. Moreover, ethologists and pig breeders may also be interested by more specific postures, such as "lying on left side", "lying on right side", "lying sternally" or "lying with udder exposed". The radar resolution must be sufficiently high to distinguish all these postures. Moreover, signal processing based on recognition of shapes in 3D radar images may be helpful to refine the classification and the detection of other postures. Note that other sensors, such as accelerometers and cameras, may be used to complete the proposed analysis of postural activity based on radar measurements. Future works will focus on fusion between data provided by these different sensors.

#### 4.3.2. Static clutter and calibration method

The calibration step of the radar setup is mandatory to mitigate the electromagnetic clutter generated by metallic bars, fences, ground, sow trough and piglets' through in the scene. Such clutter may generate false detections. One must note that the ground is composed of plastic grate panels that may

generate less clutter than concrete or metal ground. In most measurement results, a 3D reference radar image is obtained from the scanning of the radar beam in the farrowing pen in absence of the sow and piglets. However, this method may not be convenient in practice. A more suitable solution may consist in generating the 3D reference image by performing the beam scanning for a known and constant position and posture of the sow (for example, a lying posture next to the fences). This calibration approach was successfully applied for the monitoring of sows 015203, 015236 and 014648. Results are reported in Table 2. We observe that it has no impact on the postural classification results (Fig 13), since the reference "*lying*" posture was properly chosen without altering the detections of "*standing and transition*" postures.

#### 4.3.3. Time-varying clutter: piglets and humans

Time-varying electromagnetic clutter is a set of variable undesirable radar echoes which cannot be mitigated by the above-described calibration technique. This clutter, which may generate false detections, can be generated by the electromagnetic backscattering of the small-sized piglets that may move quickly (compared to the sow) and are more difficult to detect from the radar detection algorithm than larger animals. However, detection is possible if piglets are gathered and at rest. In that specific case, we can remove the undesirable 3D clusters generated by the piglets from selecting the set of clusters having the highest number of voxels. Human operators may also be detected by the radar during an experiment, for example during an intervention next to or inside the farrowing pen. In that case, the radar echoes of such targets may be easily mitigated from selecting detections that are inside the edges of the farrowing pen with the maximal height of  $z_{lim}=1.1\text{m}$ .

## 5. Conclusion

The proposed method based on a millimeter-wave radar imaging system for monitoring the postural activity of sows provides promising results. It allows both the detection of the 3D position of the sow and the classification of standing and lying postures with a mean balanced accuracy greater than 90% at cost of a few training radar data. The simultaneous prediction of sow postural activity and position inside the farrowing pen by the radar system may be used advantageously by scientists and engineers. Precision and increased number of different detected postures can be improved in future works by the fusion of radar data and accelerometer data. The

radar-based technique was applied here in a cluttered environment inside farrowing pens, but it may be extended to monitor pigs under other housing conditions. The well-documented long detection range capability of FM-CW radars (compared, e.g., to optical cameras) may be exploited to detect and study livestock outdoor in open and large areas.

## Acknowledgments

This work is part of the National France Future Élevage Carnot Network (WHAT-SOW project). Authors would like to thank the team of the pig breeding unit of UE INRAE GenESI led by W. Hebrard. Authors would like also to thank the electrical and automation team of INRAe GenPHySe, in particular E. Ricard for his expert advice, as well as M. Aletru and G. Delosières for the 3D printing of mechanical pieces.

## Appendix A. Supplementary Data

See video file *radar\_detections.mp4* in supplementary materials.

## References

- Ahmadi, B.V., Stott, A., Baxter, E., Lawrence, A., Edwards, S., 2011. Animal welfare and economic optimisation of farrowing systems. *Animal Welfare* 20, 57–67. doi:10.1017/S0962728600002438.
- Benaissa, S., Tuyttens, F.A., Plets, D., Cattrysse, H., Martens, L., Vandaele, L., Joseph, W., Sonck, B., 2019. Classification of ingestive-related cow behaviours using rumiwatch halter and neck-mounted accelerometers. *Applied Animal Behaviour Science* 211, 9–16. URL: <https://www.sciencedirect.com/science/article/pii/S016815911830409X>, doi:<https://doi.org/10.1016/j.applanim.2018.12.003>.
- Bonneau, M., Benet, B., Labrune, Y., Bailly, J., Ricard, E., Canario, L., 2021. Predicting sow postures from video images: Comparison of convolutional neural networks and segmentation combined with support vector machines under various training and testing setups. *Biosystems Engineering* 212, 19–29. doi:<https://doi.org/10.1016/j.biosystemseng.2021.09.014>.
- Canario, L., Labrune, Y., Bompa, J.F., Billon, Y., Ravon, L., Reignier, S., Bailly, J., Bonneau, M., Ricard, E., 2019. Development and validation of an embedded tool to measure postural activity of lactating sows, in:

70. Annual Meeting of the European Association for Animal Production (EAAP), Wageningen Academic Publishers, Ghent, Belgium. p. 717 p.

Comaniciu, D., Meer, P., 2002. Mean shift: a robust approach toward feature space analysis. *IEEE Transactions on Pattern Analysis and Machine Intelligence* 24, 603–619. doi:10.1109/34.1000236.

Del-Rey-Maestre, N., Jarabo-Amores, M.P., Mata-Moya, D., Almodóvar-Hernández, A., Gómez-del Hoyo, P.J., 2021. A DVB-T Passive Radar 3D-Detection Approach Based on Non-Coherent Spatial Integration, in: 2020 17th European Radar Conference (EuRAD), pp. 362–365. doi:10.1109/EuRAD48048.2021.00099.

Dore, A., Lihoreau, M., Bailly, J., Billon, Y., Bompa, J.F., Ricard, E., Henry, D., Canario, L., Aubert, H., 2022. Automated detection of sow posture changes with millimeter-wave radars and deep learning. *bioRxiv* doi:10.1101/2022.04.13.488188.

Dore, A., Pasquaretta, C., Henry, D., Ricard, E., Bompa, J.F., Bonneau, M., Boissy, A., Hazard, D., Lihoreau, M., Aubert, H., 2021. A Non-Invasive Millimetre-Wave Radar Sensor for Automated Behavioural Tracking in Precision Farming - Application to Sheep Husbandry. *Sensors* 21. doi:10.3390/s21238140.

Edwards, S., 2002. Perinatal mortality in the pig: environmental or physiological solutions? *Livestock Production Science* 78, 3–12. doi:https://doi.org/10.1016/S0301-6226(02)00180-X. peri- and Post-Natal Mortality in the Pig.

Girardie, O., Bonneau, M., Billon, Y., Bailly, J., David, I., Canario, L., 2023. Analysis of image-based sow activity patterns reveals several associations with piglet survival and early growth. *Frontiers in Veterinary Science* 9. doi:10.3389/fvets.2022.1051284.

Henry, D., Aubert, H., Ricard, E., Hazard, D., Lihoreau, M., 2018. Automated Monitoring of Livestock Behavior Using Frequency-Modulated Continuous-Wave Radars. *Progress In Electromagnetics Research M* 69, 151–160. doi:doi:10.2528/PIERM18040404.

INRAS, . INRAS Radarbook2. <https://inras.at/en/radarbook2/>. Accessed: 2022-12-08.

- Kuang, C., Wang, C., Wen, B., Hou, Y., Lai, Y., 2020. An Improved CA-CFAR Method for Ship Target Detection in Strong Clutter Using UHF Radar. *IEEE Signal Processing Letters* 27, 1445–1449. doi:10.1109/LSP.2020.3015682.
- Küster, S., Kardel, M., Ammer, S., Brünger, J., Koch, R., Traulsen, I., 2020. Usage of computer vision analysis for automatic detection of activity changes in sows during final gestation. *Computers and Electronics in Agriculture* 169, 105177. doi:https://doi.org/10.1016/j.compag.2019.105177.
- Li, M., Stolz, M., Feng, Z., Kunert, M., Henze, R., Küçükay, F., 2018. An adaptive 3d grid-based clustering algorithm for automotive high resolution radar sensor, in: 2018 IEEE International Conference on Vehicular Electronics and Safety (ICVES), pp. 1–7. doi:10.1109/ICVES.2018.8519483.
- Liu, L., Zhou, J., Zhang, B., Dai, S., Shen, M., 2022. Visual detection on posture transformation characteristics of sows in late gestation based on libra r-cnn. *Biosystems Engineering* 223, 219–231. doi:https://doi.org/10.1016/j.biosystemseng.2022.09.003.
- Lu, L., Mao, L., Wang, J., Gong, W., 2022. Reserve sow pose recognition based on improved yolov4, in: 2022 IEEE Asia-Pacific Conference on Image Processing, Electronics and Computers (IPEC), pp. 1538–1546. doi:10.1109/IPEC54454.2022.9777590.
- Manteuffel, C., 2019. Parturition detection in sows as test case for measuring activity behaviour in farm animals by means of radar sensors. *Biosystems Engineering* 184, 200–206. doi:https://doi.org/10.1016/j.biosystemseng.2019.06.018.
- Matthews, S.G., Miller, A.L., Plötz, T., Kyriazakis, I., 2017. Automated tracking to measure behavioural changes in pigs for health and welfare monitoring. *Scientific Reports* 7. doi:https://doi.org/10.1038/s41598-017-17451-6.
- Palffy, A., Dong, J., Kooij, J.F.P., Gavrila, D.M., 2020. Cnn based road user detection using the 3d radar cube. *IEEE Robotics and Automation Letters* 5, 1263–1270. doi:10.1109/LRA.2020.2967272.
- Pastell, M., Hietaoja, J., Yun, J., Tiisanen, J., Valros, A., 2016. Predicting farrowing of sows housed in crates and pens using accelerometers and cusum charts. *Computers and Electronics in Agriculture* 127, 197–203. doi:https://doi.org/10.1016/j.compag.2016.06.009.

- Pedregosa, F., Varoquaux, G., Gramfort, A., Michel, V., Thirion, B., Grisel, O., Blondel, M., Prettenhofer, P., Weiss, R., Dubourg, V., Vanderplas, J., Passos, A., Cournapeau, D., Brucher, M., Perrot, M., Duchesnay, E., 2011. Scikit-learn: Machine Learning in Python. *Journal of Machine Learning Research* 12, 2825–2830.
- Piper, S., 1993. Receiver frequency resolution for range resolution in homodyne FMCW radar, in: *Conference Proceedings National Telesystems Conference 1993*, pp. 169–173. doi:10.1109/NTC.1993.292991.
- Raj, S., Ghosh, D., 2020. Improved and optimal dbscan for embedded applications using high-resolution automotive radar, in: *2020 21st International Radar Symposium (IRS)*, pp. 343–346. doi:10.23919/IRS48640.2020.9253774.
- Riaboff, L., Shalloo, L., Smeaton, A., Couvreur, S., Madouasse, A., Keane, M., 2022. Predicting livestock behaviour using accelerometers: A systematic review of processing techniques for ruminant behaviour prediction from raw accelerometer data. *Computers and Electronics in Agriculture* 192, 106610. URL: <https://www.sciencedirect.com/science/article/pii/S016816992100627X>, doi:<https://doi.org/10.1016/j.compag.2021.106610>.
- Richards, M.A., 2014. *Fundamentals of Radar Signal Processing*. McGraw Hill Education.
- Ringgenberg, N., Bergeron, R., Devillers, N., 2010. Validation of accelerometers to automatically record sow postures and stepping behaviour. *Applied Animal Behaviour Science* 128, 37–44. doi:<https://doi.org/10.1016/j.applanim.2010.09.018>.
- Tharwat, A., 2016. Linear vs. quadratic discriminant analysis classifier: a tutorial. *International Journal of Applied Pattern Recognition* 3, 145–180. doi:10.1504/IJAPR.2016.079050. pMID: 79050.
- Wagner, T., Feger, R., Stelzer, A., 2016. A fast grid-based clustering algorithm for range/Doppler/DoA measurements, in: *2016 European Radar Conference (EuRAD)*, pp. 105–108.
- Wagner, T., Feger, R., Stelzer, A., 2017. Radar Signal Processing for Jointly Estimating Tracks and Micro-Doppler Signatures. *IEEE Access* 5, 1220–1238. doi:10.1109/ACCESS.2017.2667720.

- Wang, S., Herschel, R., 2022. Fast 3D-CFAR for Drone Detection with MIMO Radars, in: 2021 18th European Radar Conference (EuRAD), pp. 209–212. doi:10.23919/EuRAD50154.2022.9784486.
- Wang, Y., Zhi, J., Shen, W., Lin, Y., Li, Y., 2022. CFAR-Based Point Cloud Extraction Method for Circular Scanning Ground-Based SAR 3D Image, in: 2022 IEEE 5th International Conference on Computer and Communication Engineering Technology (CCET), pp. 106–109. doi:10.1109/CCET55412.2022.9906372.
- Xu, J., Zhou, S., Xu, A., Ye, J., Zhao, A., 2022. Automatic scoring of postures in grouped pigs using depth image and cnn-svm. *Computers and Electronics in Agriculture* 194, 106746. doi:https://doi.org/10.1016/j.compag.2022.106746.
- Yang, A., Huang, H., Zhu, X., Yang, X., Chen, P., Li, S., Xue, Y., 2018. Automatic recognition of sow nursing behaviour using deep learning-based segmentation and spatial and temporal features. *Biosystems Engineering* 175, 133–145. doi:https://doi.org/10.1016/j.biosystemseng.2018.09.011.
- Zheng, C., Zhu, X., Yang, X., Wang, L., Tu, S., Xue, Y., 2018. Automatic recognition of lactating sow postures from depth images by deep learning detector. *Computers and Electronics in Agriculture* 147, 51–63. doi:https://doi.org/10.1016/j.compag.2018.01.023.